

Optical decoherence, spectroscopy, and magnetic g tensors for the $1.5\text{-}\mu\text{m}$ ${}^4I_{15/2} - {}^4I_{13/2}$ transitions of Er^{3+} dopants at the C_2 -symmetry site in Y_2O_3

Thomas Böttger^{✉,*}, T. L. Harris, G. D. Reinemer[✉], C. W. Thiel, and R. L. Cone

Department of Physics and Spectrum Laboratory, Montana State University, Bozeman, Montana 59717, USA



(Received 10 January 2024; accepted 25 June 2024; published 17 July 2024)

Erbium-doped solids are a promising platform for quantum technology due to the Er^{3+} $1.5\text{-}\mu\text{m}$ optical transition in the telecom C band that can offer long coherence times. To characterize the intrinsic C_2 site of Er^{3+} in Y_2O_3 for quantum information and photonic signal-processing applications, absorption and site-selective fluorescence spectroscopy were used to assign the $\text{Er}^{3+} {}^4I_{15/2} \leftrightarrow {}^4I_{13/2}$ transitions. The lowest-to-lowest transition occurs at 1535.608 nm and laser absorption determined an inhomogeneous linewidth of 780 MHz in a 0.005% -doped crystal at 3.4 K . Time-resolved fluorescence established an upper limit for the excited-state lifetime of 8.5 ms . Angular-dependent Zeeman absorption was used to determine ground- and excited-state g tensors. The C_2 -site g tensor components for the ground state are $g_x = 1.60$, $g_y = 4.71$, and $g_z = 11.93$ with a tipping angle of $\alpha = 2.06^\circ$, whereas for the excited state the components are $g_x = 1.08$, $g_y = 4.36$, and $g_z = 10.07$ with a tipping angle of $\alpha = -11.7^\circ$. Optical decoherence can be suppressed by the application of a magnetic field parallel to (111) crystal axes where all C_2 sites become nearly magnetically equivalent with large g values so that spin flips of neighboring Er^{3+} ions can be simultaneously suppressed. Using this magnetic field direction, two-pulse photon echoes gave a homogeneous linewidth of 5 kHz for an applied magnetic field of 0.5 T , narrowing and saturating at 2.5 kHz at 3.5 T . Decoherence over intermediate magnetic fields was described by spectral diffusion due to Er^{3+} - Er^{3+} magnetic dipole interactions driven by the direct phonon process. With $\text{Er}^{3+}:\text{Y}_2\text{O}_3$ absorption at a convenient telecom laser wavelength and the ability to fabricate waveguides, our study suggests that this is a promising material system for quantum information and spectral hole-burning signal-processing applications.

DOI: [10.1103/PhysRevB.110.045132](https://doi.org/10.1103/PhysRevB.110.045132)

I. INTRODUCTION

Experimental demonstrations and theoretical analysis by groups around the world have shown that rare-earth ions (REI) embedded in crystal hosts are some of the most promising candidates to meet the requirements for multimode optical quantum memories as well as quantum transducers for reversible microwave to optical conversion, both being key components for many applications in quantum information science (QIS) [1–10]. These same REI-doped materials can also be used in combination with conventional holography to create spectral-spatial (S2) holography. This S2 holography is capable of optical signal processing, range-Doppler radar signal processing, and spectrum analysis at high bandwidths well into the gigahertz (GHz) regime and beyond the bandwidth of related electronic signal processing [11–16]. Narrow spectral holes that can be burned into rare-earth absorption lines have also enabled laser frequency stabilization [17,18] competitive with state-of-the-art flywheel oscillators [19], as well as laser linewidth narrowing [7,20], and spectral filtering [21,22].

These QIS and spectral hole-burning (SHB) applications are possible due to the unique properties of REI-doped materials such as long optical and spin coherence lifetimes, the possibility of controlling line broadening and interactions by external electric and magnetic fields, simultaneous

storage of many photons and quantum states, efficient photon interactions, optically accessible nuclear spin states for long-term storage mechanisms, and the potential to interface with superconducting qubits or other physical systems via microwave-to-optical transduction [23–28]. The phenomenon of SHB enables spectrally distinct ensembles of ions within the high-density environment to be individually manipulated and interrogated, leading to the potential for 10^6 or more frequency-multiplexed storage channels in addition to the large intrinsic spatial multiplexing capacity of volumetric storage. Quantum states encoded onto temporal, spectral, polarization, and spatial modes of light, true-time delay signals for phased arrays, as well as correlation and convolution of optical pulse trains at multi-GHz bandwidths, can all be stored and recalled using the massive information handling capacity of REI-doped crystals [3,5–7,29].

Achieving the full potential of these materials requires advances in our fundamental understanding and practical control of the physical processes that govern ion-ion, ion-spin, and ion-lattice interactions within the solid-state environment. Often materials can be “engineered” by adjusting their chemical composition, dopant concentration, crystal orientation, operating temperature, magnetic field strength and direction, and postgrowth processing. The combination and interplay of these variables set up a very large parameter space within which to find the optimum conditions. For example, one issue with REI-doped materials with strong intrinsic paramagnetism, such as Er^{3+} , is the coupling of the optical and

*Contact author: thomas.bottger@montana.edu

spin transitions to local magnetic fields caused by nuclear and electronic spin fluctuations in its environment. This coupling contributes to decoherence and dynamic line broadening, an effect known as “spectral diffusion” [7,30,31]. Spectral diffusion in Er^{3+} -doped systems can be frozen out with an appropriate applied magnetic field, lowering the temperature for example with a dilution refrigerator [32,33], or by diluting the dopant concentration or codoping with other ions [30,34,35].

Realization of practical solid-state quantum memories and SHB signal-processing devices depends on identifying materials that offer a demanding combination of physical properties along with massively parallel channel scalability to provide required data rates, for example in secure communication networks or in range-Doppler radar signal processing. Erbium-doped materials are of special importance as they facilitate interfacing with the existing optical fiber network and hardware. The material Y_2O_3 is a high-quality laser host material [36] and also known to be suitable for fabrication of waveguides [37]. Waveguides potentially offer the opportunity for chip-scale integration and optoelectronic engineering of a complete quantum memory system including generation, transport, storage, recall, and detection of entangled photons [8,38–40].

Coherence and spin relaxation can be strongly affected by chemical, mechanical, or thermal processing of REI materials [41–44]. Recent advances in Er^{3+} - and Eu^{3+} -doped Y_2O_3 nanoparticles, thin films, and synthesized ceramics revealed bulk crystal properties can be achieved or recovered in these embodiments [21,38,45–47], particularly at sub-Kelvin temperatures [48–50].

The host material Y_2O_3 , when doped with Er^{3+} , exhibits resonant optical transitions at $1.54\ \mu\text{m}$ that enable spectral hole burning at cryogenic temperatures. Similar to Y_2SiO_5 [51], the Y_2O_3 host lattice contributes minimally to the fluctuating local field. The constituent nuclear magnetic moments are either zero in the case of ^{16}O , very small in the case of ^{89}Y with a moment of $-0.14\ \mu\text{N}$, or of low enough isotopic abundance as not to be of consequence in the case of 0.04% abundant ^{17}O with a moment of $-1.89\ \mu\text{N}$. Indeed, a previous study on single-crystal $\text{Eu}^{3+}:\text{Y}_2\text{O}_3$ showed excellent coherence characteristics with sub-kHz homogeneous linewidth [52].

However, the material $\text{Er}^{3+}:\text{Y}_2\text{O}_3$ is relatively unexplored despite its telecom transition as compared to other materials such as Y_2SiO_5 , motivating this study to characterize the Er^{3+} $^4I_{15/2}$ and $^4I_{13/2}$ energy levels in Y_2O_3 and their magnetic and decoherence properties so that the system may be developed for QIS and SHB applications.

The Er^{3+} ions substitute for two inequivalent crystallographic Y^{3+} sites, one with C_2 and the other with $\text{C}_{3i}-(\text{S}_6)$ -point symmetry. This paper focuses on the C_2 site, while a follow-up paper will report our detailed results for the C_{3i} site [53]. Absorption measurements were used to study the excited-state crystal-field levels, and site-selective fluorescence and fluorescence excitation allowed us to confidently separate and characterize the $^4I_{13/2}$ excited and $^4I_{15/2}$ ground-state-level structure for the two Er^{3+} crystallographic sites. Time-resolved fluorescence spectroscopy was used to measure the excited-state lifetime, which limits the maximum

achievable decoherence time for the ions. Decoherence in $\text{Er}^{3+}:\text{Y}_2\text{O}_3$ primarily arises from spectral diffusion caused by Er^{3+} ion spin-spin interactions, which can be controlled through the application of a magnetic field. To find optimal directions for applying the magnetic field, the g tensors of both the ground and excited states are needed [54]. The ground-state $^4I_{15/2}$ (Z_1) g tensor has been previously determined by Schäfer and Scheller [55] through electron paramagnetic resonance spectroscopy (EPR). In this work, we used high-resolution Zeeman laser absorption experiments to obtain the g tensors for both states. Our ground-state g tensor agrees well with the earlier EPR work. The excited-state g tensor is not accessible through EPR, so our measured excited-state g tensor provides valuable information. From the measured angle-dependent g values, two preferred field orientations for minimizing optical decoherence were identified and studied using two-pulse photon-echo experiments to measure the optical dephasing as a function of magnetic field strength.

II. MATERIAL PROPERTIES OF $\text{Er}^{3+}:\text{Y}_2\text{O}_3$

Historically, growing high-quality bulk Y_2O_3 was challenging. For our study, high-quality 0.05 and 0.005% $\text{Er}^{3+}:\text{Y}_2\text{O}_3$ single crystals were successfully grown by Scientific Materials Corporation/Teledyne-FLIR of Bozeman, Montana, using a high-temperature top-seeded solution growth technique. Samples were oriented with Laue x-ray diffraction and polished with surfaces parallel to (001), (110), and (111) planes. Sample thicknesses varied between 3 and $12\ \text{mm}$ depending on the requirements for individual measurements.

The crystal Y_2O_3 has cubic symmetry described by space group $Ia\bar{3}$ (International Tables for Crystallography No. 206). The unit cell contains 16 formula units with a lattice constant of $a = 10.6\ \text{\AA}$ [56]. Trivalent rare-earth ions substitute for Y^{3+} in the lattice at two crystallographically inequivalent lattice sites at the Wyckoff d -site position with C_2 -point symmetry and the Wyckoff b -site position with $\text{C}_{3i}-(\text{S}_6)$ -point symmetries, with a relative site density of 3:1, respectively. The Er^{3+} ions, with an ionic radius nominally the same as Y^{3+} , substitute into both Y^{3+} sites nonpreferentially according to Mandel [57]. Within a unit cell, the combination of the space group and the site point group gives rise to a multisite structure exhibiting multiple magnetically inequivalent orientations. For the C_2 sites, there are six magnetically inequivalent subgroups of ions with their local C_2 rotation axes aligned along the six different (001) lattice directions. The material density is $5.010\ \text{g/cm}^3$, the concentration of Y^{3+} C_2 sites is $1.603 \times 10^{22}\ \text{ions/cm}^3$, and the estimated index of refraction is 1.81 at $1.5\ \mu\text{m}$ [58].

The magnetic properties for a particular Er^{3+} site are characterized by three principal g values and three Euler angles that locate magnetic principal axes relative to crystallographic axes. Crystal symmetry may simplify the measurement of one or more of these parameters. The C_2 and C_{3i} sites have different magnetic properties reflected in the different anisotropies of their g tensors as well as magnetic site inequivalencies relative to a magnetic field applied in an arbitrary direction. These anisotropies were utilized to confirm the overall site assignments.

For optical transitions we do not directly observe the splittings in the ground state or in the excited state. Rather, we observe the transitions between the split ground-state and excited-state Zeeman levels. Those transition energies allow determination of the principal values of the ground-state g tensor as well as the excited-state g tensor.

For the C_2 site, the unique C_2 axis is confined to the $\langle 001 \rangle$ axis of the crystal and defines the local magnetic z axis for the site. The magnetic x - and y -axes are not confined to any of the crystal axes and have been described by Schäfer and Scheller as being rotated by an angle α , defined as the angle between the $+x$ axis and the $\langle 100 \rangle$ crystal axis. [55] The same terminology can be applied for excited states, although the α value is typically different for each electronic state. For the C_2 site there are thus four free parameters: g_x , g_y , g_z , and α for each state, and the 24 C_2 sites per unit cell can be reduced to 6 magnetically inequivalent orientations, each of which gives a different but related angular-dependent Zeeman splitting.

Upper limits for g values are determined by $2J$ times the Lande g_J factor, which is 1.2 for $^4I_{15/2}$ levels and 1.1 for $^4I_{13/2}$ levels, giving maximum principal g values of 18 and 14.4 for ground- and excited-state multiplets, respectively.

III. ABSORPTION AND FLUORESCENCE

Absorption and fluorescence measurements were carried out between 1.5 and 10 K in a liquid helium cryostat. The experimental apparatus was the same as described in Ref. [59]. Absorption scans were recorded using a tungsten halogen light source focused onto the sample. The transmitted signal through the crystal was analyzed by a SPEX 1000M 1-m monochromator with a 600-grooves per mm grating blazed at 1500 nm and with an inverse resolution of 1.6 nm/mm. Glass color filters were employed in front of the cryostat to avoid heating the sample and to eliminate spectral features from higher grating orders. A liquid nitrogen-cooled germanium detector was used for detection. Entrance and exit slits were typically set at 20 μm for a bandpass of 0.14 cm^{-1} .

Higher-resolution measurements were provided by laser absorption spectroscopy using an experimental setup as described in Ref. [59]. In these measurements, a home-made single-frequency 1.5- μm tunable external cavity diode laser (ECDL) was scanned over the region of interest and the transmitted signal through the crystal was captured with an amplified InGaAs photodetector. The laser was tunable between 1505 and 1565 nm with a jitter-limited linewidth of <200 kHz, and an output power of ~ 1.8 mW was used. By tuning the laser cavity, mode-hop free continuous linear frequency scans of 47 GHz were achieved at a 10-Hz repetition rate.

A. Absorption spectroscopy and the $^4I_{13/2}$ level structure

Broadband absorption scans were carried out on the Er^{3+} $^4I_{15/2} \rightarrow ^4I_{13/2}$ transitions over the 6450–6900 cm^{-1} (1450–1550 nm) region using a 3.12-mm-thick 0.05% $\text{Er}^{3+}:\text{Y}_2\text{O}_3$ crystal at a temperature of $T = 2$ K. The absorption spectrum in Fig. 1 reveals a total of 12 absorption lines labeled A to L with increasing energy. Since only the lowest $^4I_{15/2}$ crystal-field level is populated at 2 K, each absorption line

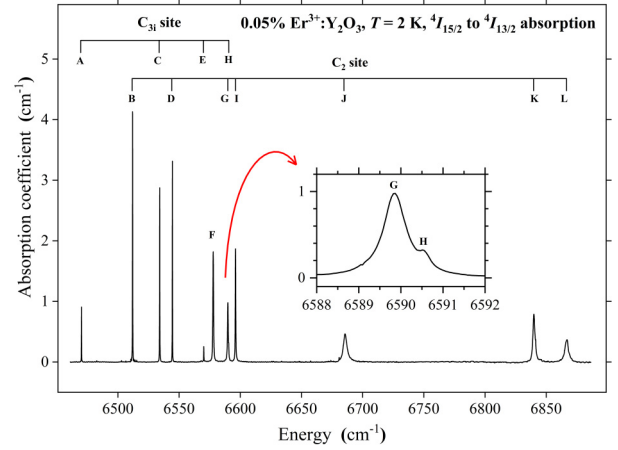


FIG. 1. Absorption spectrum of the $^4I_{15/2} \rightarrow ^4I_{13/2}$ transitions in 0.05% $\text{Er}^{3+}:\text{Y}_2\text{O}_3$ at 2 K showing 12 lines labeled A–L. Assignment of these lines to specific sites was deduced from site-selective fluorescence as described in the text. The B, D, F, I, J, K, and L lines have been assigned as originating from the C_2 site and the A, C, E, and H lines originating from the C_{3i} site. The origin of the F line is unknown.

corresponds to a unique $^4I_{13/2}$ crystal-field level. For the $J = 13/2$ multiplet, seven absorption lines are expected for each inequivalent Er^{3+} site, with the observed absorption lines originating from the overlapping spectra from the two different crystallographic sites. All transitions are allowed for the C_2 - and C_{3i} -site symmetries, with C_2 -site transitions composed of mixed electric and magnetic dipole while C_{3i} -site transitions are purely magnetic dipole. Following the usual convention, we will label ground-state $^4I_{15/2}$ crystal-field levels $Z_1 - Z_8$ with Z_1 denoting the lowest energy, and the $^4I_{13/2}$ excited-state crystal-field levels labeled $Y_1 - Y_7$ with Y_1 denoting the lowest energy.

As described in the later sections, the Er^{3+} sites were confirmed to be the C_2 site and C_{3i} site and each transition was assigned to the corresponding site as labeled in Fig. 1. The B, D, G, I, J, K, and L lines match the C_2 -site $Y_1 - Y_7$ levels reported by Kisliuk and Gruber [60] and Chang [61]. On the other hand, no literature reference was found for the C_{3i} -site transitions labeled A, C, E, and H, so our values provide information that will be analyzed in a follow-up paper focusing on the C_{3i} site [53].

Also evident from Fig. 1 are the progressively increasing absorption linewidths for the C_2 -site (C_{3i} -site) $^4I_{15/2} \rightarrow ^4I_{13/2}$ transitions as energy increases within the $J = 13/2$ manifold, going from 6.4 to 105 GHz (3.0 to 16.8 GHz) due to lifetime broadening arising from spontaneous phonon emission from the upper to the lower crystal-field levels. The narrowest absorption linewidths from Fig. 1 were limited by the resolution of the spectrometer, requiring laser absorption techniques for precise linewidth measurements, as described in Sec. III D.

B. Site-selective fluorescence spectroscopy and the $^4I_{15/2}$ level structure

Each $^4I_{13/2}$ level determined from Fig. 1 was assigned unambiguously to a specific crystallographic site using

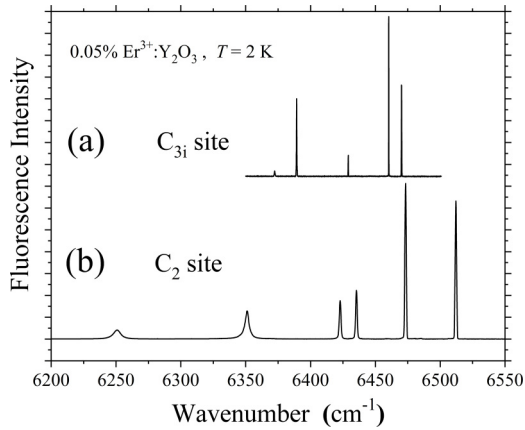


FIG. 2. Site-selective fluorescence excitation spectra of the ${}^4I_{13/2}$ (Y_1) \leftrightarrow ${}^4I_{15/2}$ (Z_n) transitions in 0.005% $\text{Er}^{3+}:\text{Y}_2\text{O}_3$ at 2 K. Two distinct spectra are observed for excitation of the different absorption lines. Each spectrum corresponds to fluorescence from the lowest ${}^4I_{13/2}$ crystal-field level of a specific lattice site to all the corresponding ${}^4I_{15/2}$ levels. The C_{3i} -site fluorescence intensity is shown magnified 5 times relative to the C_2 -site fluorescence.

site-selective fluorescence experiments that also provided unambiguous level assignments for the ${}^4I_{15/2}$ J manifold for each site. When an individual line in the absorption spectrum of Fig. 1 was excited at $T = 2$ K, only one of two distinct fluorescence spectra was observed. Those two distinct fluorescence spectra are associated with the two crystallographic sites and are shown in Fig. 2. Orientation-dependent Zeeman effect measurements described in Sec. IV were used to confirm the C_2 - and C_{3i} -site symmetry of the two observed Er^{3+} sites. The tuning range of the ECDL limited excitation to absorption lines up to line I; hence, the lines labeled J , K , and L in Fig. 1 could not be assigned using our apparatus, but they were identified by comparing to values found in the literature, as discussed below. The spectrum shown in Fig. 2(a) has the highest energy transition at 6512 cm^{-1} and was obtained by exciting lines B , D , G , and I with the ECDL. On the other hand, the spectrum shown in Fig. 2(b) with the highest transition at 6470 cm^{-1} was obtained by exciting lines A , C , E , and H . Exciting line F (6580 cm^{-1}) shown in the absorption spectrum in Fig. 1 did not result in any observable emission, nor did its absorption strength scale with erbium dopant concentration. Hence, we concluded that line F is not associated with the Er^{3+} transitions, and that its origin needs further investigation. Lines G and H were barely resolvable in

the absorption spectrum and are shown to be only 0.8 cm^{-1} apart. An expanded view of these lines is provided in the inset of Fig. 1. They were assigned by setting the spectrometer at the emission lines of either spectrum shown in Fig. 2(a) or Fig. 2(b) and scanning the laser while monitoring the emission intensity.

The spectrum shown in Fig. 2(b) matches that expected from the Er^{3+} C_2 -site values reported by Kisliuk and Gruber [60] and Gruber *et al.* [62]. Consequently, lines J , K and L in Fig. 1 are assigned to the C_2 site.

No literature references were found for the site-selective ${}^4I_{13/2}$ fluorescence shown in Fig. 2(a). These spectra contain information associated with the C_{3i} site. This assignment has been confirmed by angle-dependent Zeeman laser absorption measurements to be reported in a separate paper [53]. Dean and Bloor's far-infrared measurements reported the same Z_3 and Z_4 C_{3i} -level energies deduced from our spectrum, further validating our C_{3i} -site designation for these lines [63].

The C_2 -site crystal-field level structure of $\text{Er}^{3+}:\text{Y}_2\text{O}_3$ determined from absorption and site-selective fluorescence experiments is summarized in Table I. All energies were obtained by fitting to determine the observed line centers. While our ground-state levels agree very well with the work of [62], we did not observe the Z_8 level and measured the Z_7 level at 500 cm^{-1} , which is right between Gruber *et al.*'s measured Z_7 level at 490 cm^{-1} and Z_8 level at 510 cm^{-1} .

C. Fluorescence lifetimes

Knowledge of the excited-state lifetime T_1 of the lowest ${}^4I_{13/2}$ state is important as it establishes an upper bound for the achievable T_2 decoherence lifetime through the relation $T_2 \leq 2T_1$ as well as the lifetime of optical spectral population gratings, such as Atomic Frequency Comb quantum memories. The experimental apparatus for measuring fluorescence was identical to Ref. [59]. A nitrogen-cooled Hamamatsu R3809U-69 near-infrared photomultiplier tube was used with the monochromator tuned to the ${}^4I_{13/2}(Y_1) \rightarrow {}^4I_{15/2}(Z_1)$ transition. Fluorescence from ${}^4I_{13/2}(Y_1)$ was measured following pulsed-laser excitation of the ${}^4I_{15/2}(Z_1) \rightarrow {}^4I_{13/2}(Y_2)$ transition, as the ${}^4I_{13/2}(Y_2)$ rapidly relaxes nonradiatively to the ${}^4I_{13/2}(Y_1)$ state before fluorescing to the ${}^4I_{15/2}$ levels. The laser pulse duration was 2.5 ms. Excitation of the C_2 site was at 6544.7 cm^{-1} and the detection was recorded at 6512.1 cm^{-1} by the spectrometer. To minimize the effects of radiation

TABLE I. Observed energy levels for the ${}^4I_{15/2}$ and ${}^4I_{13/2}$ multiplets of Er^{3+} at the C_2 site in Y_2O_3 . Note that level Z_8 was not observed in these measurements.

Ground state	Level	Energy (cm^{-1})	Excited state	Level	Energy (cm^{-1})
${}^4I_{15/2}$	Z_1	0	${}^4I_{13/2}$	Y_1	6512.1
	Z_2	39.5		Y_2	6544.5
	Z_3	77.4		Y_3	6589.8
	Z_4	90		Y_4	6596.1
	Z_5	161.8		Y_5	6686.4
	Z_6	261.8		Y_6	6841
	Z_7	500		Y_7	6868

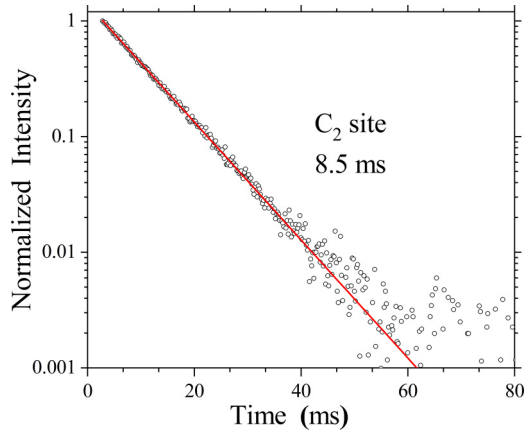


FIG. 3. Excited-state lifetime measurement of Er^{3+} -occupied C_2 site in Y_2O_3 . The graph shows the fluorescence decay curve and least-squares fit to the data. Excitation of the C_2 site at 6544.7 cm^{-1} and detection at 6512.1 cm^{-1} yielded an upper-state lifetime of $(8.5 \pm 0.1) \text{ ms}$.

trapping, a low-concentration $0.005\% \text{ Er}^{3+}:\text{Y}_2\text{O}_3$ crystal was used. Measurements were carried out at a temperature of 1.5 K to avoid significant population of ${}^4I_{13/2}$ levels other than the lowest-energy Y_1 excited level.

A typical normalized single-shot fluorescence decay is shown in Fig. 3. The straight line corresponds to an exponential least-square fit yielding a fluorescence lifetime of $T_1 = 8.5 \pm 0.1 \text{ ms}$, which agrees well with the value of 8 ms measured by Dieke for $0.2\% \text{ Er}^{3+}:\text{Y}_2\text{O}_3$ at a temperature of 77 K [64].

A common problem with fluorescence decay measurements is radiative energy trapping, during which the emitted resonant photon is reabsorbed (trapped) and then reemitted, slowing down the overall observed fluorescence decay and hence leading to apparent fluorescence lifetimes that are longer than the true excited-state lifetime T_1 [65,66]. Radiation trapping may contribute to the measured lifetimes, so the numbers reported here should be understood as an upper limit for T_1 . Time-resolved spectral hole-decay measurements can be used to avoid the effect of radiation trapping, as we have shown in other systems [67,68].

D. Laser absorption

To accurately measure the inhomogeneous linewidth for the C_2 site, a 3.46-mm -thick $0.005\% \text{ Er}^{3+}:\text{Y}_2\text{O}_3$ crystal was used. The crystal was placed inside a Montana Instruments C_2 Cryostation in zero magnetic field at a temperature of $T = 3.4 \text{ K}$. The ECDL laser light was propagated through the crystal without focusing. Transmitted light was detected with a Newport 2033 large-area germanium photodetector. Laser absorption spectra were recorded by scanning the ECDL over the spectral region of interest. To calibrate the spectra, we simultaneously recorded a fiber Fabry-Perot transmission spectrum with a free spectral range of 49.42 MHz .

Figure 4 shows the unpolarized laser absorption spectrum for the C_2 site ${}^4I_{15/2}(Z_1) \rightarrow {}^4I_{13/2}(Y_1)$ transition in 0.005%

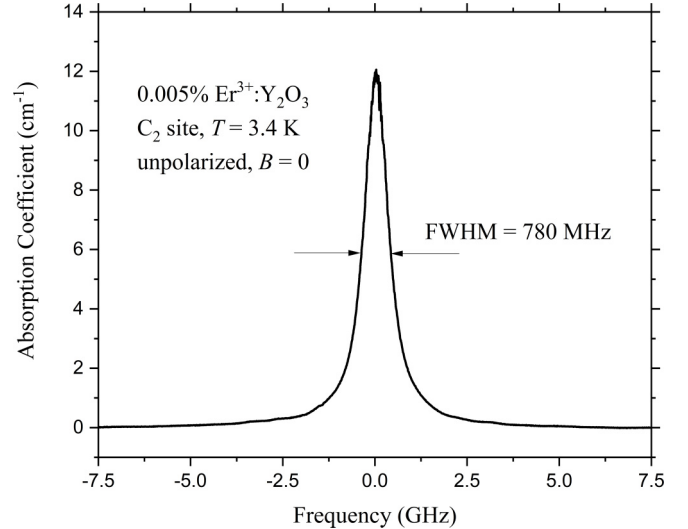


FIG. 4. Unpolarized laser absorption spectrum for the ${}^4I_{15/2}: Z_1 \rightarrow {}^4I_{13/2}: Y_1$ transition at 6512.078 cm^{-1} , or 1535.608 nm in vacuum, of Er^{3+} ions at the C_2 site in $0.005\% \text{ Er}^{3+}:\text{Y}_2\text{O}_3$ at $T = 3.4 \text{ K}$.

$\text{Er}^{3+}:\text{Y}_2\text{O}_3$ occurring at 6512.078 cm^{-1} at a temperature of 3.4 K . The inhomogeneous line shape is accurately described by a Lorentzian with full width at half maximum of 780 MHz .

IV. ZEEMAN SPECTROSCOPY

Because the magnetic moment of the Er^{3+} ions in the ground- and excited states is a key variable in achieving slow decoherence, we determined the g tensor components for the C_2 site from angle-dependent Zeeman laser spectroscopy. The goal was to identify a magnetic field direction where the g values are simultaneously maximized in the ground- as well as the excited state so that spectral diffusion by Er^{3+} spin flips may be suppressed. If the level splitting, described by the effective g value, is large compared to the available thermal energy $k_B T$, thermal populations in the upper Zeeman level are reduced and hence Er^{3+} spin flips inhibited [30,35].

A. Experiment

The g tensors for the ${}^4I_{15/2}$ and ${}^4I_{13/2}$ levels of Er^{3+} ions in the C_2 site were determined from laser absorption spectra taken while the sample was rotated in 5° increments through 120° . For this purpose, a special sample holder was built as described in Ref. [54] to rotate the sample around a horizontal axis normal to the horizontal applied magnetic field. Sample rotation was facilitated by a worm gear driven from the top of the cryostat by a vertical shaft, with the rotation angle determined from the known gear ratio. Great care was taken to properly align the sample as described in Ref. [54].

As described in Ref. [59], Zeeman measurements were greatly facilitated by using a high-precision frequency marker established by the beat note between the scanning ECDL and a second ECDL. The laser frequency of the second ECDL was manually adjusted by changing the piezovoltage applied to the feedback mirror plate, hence changing the marker frequency to overlap with one of the transitions. Blocking the scanning

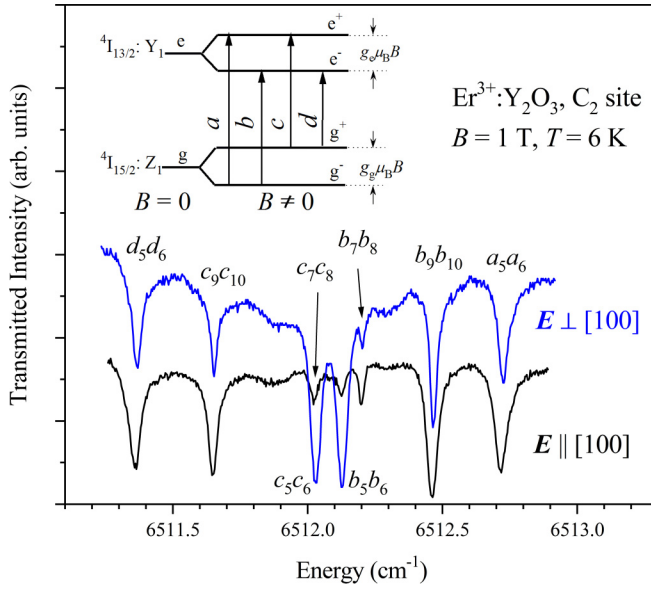


FIG. 5. Typical polarization-dependent Zeeman laser absorption spectra at $T = 6$ K in $\text{Er}^{3+}:\text{Y}_2\text{O}_3$ with $B = 1.0$ T parallel [100] in the (001) plane. Individual absorption scans have been shifted for better visibility. All inner b and c transitions and some of the outer a and d transition are visible and have been labeled with a subscript referring to individual sites. Outer a (d) transitions for ions in sites 9 and 10 lie at higher (lower) energy as indicated in the transition-labeling scheme inset and hence outside the displayed range. The inset diagram depicts the transition-labeling scheme for the four transitions between the Zeeman-split ground- $^4I_{15/2}$ and excited $^4I_{13/2}$ states.

laser allowed each absorption frequency to be measured from the second ECDL with a Burleigh WA-1500 Wavemeter to an absolute accuracy of ± 100 MHz. This method avoided any issues associated with nonlinear piezoelectric laser scans and slow laser drifts.

The magnetically inequivalent sites in $\text{Er}^{3+}:\text{Y}_2\text{O}_3$ complicate this task. When a magnetic field is applied, the cubic symmetry is broken, and the individual subgroups of sites become spectrally distinct. The splitting of the Er^{3+} $^4I_{15/2}$ (Z_1) and $^4I_{13/2}$ (Y_1) doublet levels gives rise to four transitions for each magnetically inequivalent Er^{3+} site. Identifying and tracking the individual transitions as the magnetic field direction was varied proved to be a challenging experiment as illustrated by Fig. 5, which shows typical Zeeman spectra, centered on the zero-field transition energy with $B = 1.0$ T in the (001) plane along [100]. The top and bottom traces have been measured with the polarization perpendicular and parallel to [100], respectively. Following the same labeling of sites as in Ref. [55], the subscripts have been introduced to label the individual sites. The b and c transitions for sites 5, 6, 7, and 8 strongly exhibit polarization-dependent absorption, but transition energies were never observed to shift with polarization. Two higher-energy (a_7 , a_8 and a_9 , a_{10}) and two lower-energy (d_7 , d_8 and d_9 , d_{10}) transitions were outside the laser continuous-scan range and the laser was tuned individually to these outlying transitions to measure their energies.

Following Ref. [59], we use (+) and (−) to label the upper and lower Zeeman components of the ground- and excited levels and mark the four possible transitions a , b , c , and d as

depicted in Fig. 5. The population of the upper ground-state level g^+ is temperature dependent, so observation of the c and d transitions required operation at an elevated temperature of $T = 6$ K. The temperature dependence of the line strengths was exploited to distinguish between b and c transitions as the c transition becomes weaker and the b transition stronger with decreasing temperature.

The corresponding transition energies are given by E_a for the transition energy of the ground-state (−) component to the excited-state (+) component, E_b for the (− −) transition, E_c for (+ +), and E_d for the (+ −) transition.

Several important relationships between the a , b , c , and d transitions can be deduced from Fig. 5. The energy difference between the a and c or b and d transitions allows calculation of the ground-state splitting, which in turn yields the effective ground-state g value as

$$g_g = \frac{E_a - E_c}{\mu_B B} = \frac{E_b - E_d}{\mu_B B}, \quad (1)$$

where μ_B is the Bohr magneton and B the magnetic field strength.

Similarly, the excited-state effective g value can be found from the energy difference between the a and b or c and d transitions as

$$g_e = \frac{E_a - E_b}{\mu_B B} = \frac{E_c - E_d}{\mu_B B}. \quad (2)$$

Furthermore, the energy difference between the b and c transitions gives the difference between the ground- and excited-state splittings.

When tracking individual lines as a function of magnetic field direction, it was useful to calculate the expected transition energies for each site. The a and d transition energies are given by

$$E_i^{(a,d)} = E_0 \pm \frac{\mu_B}{2} ({}^g g_i + {}^e g_i) B, \quad (3)$$

where E_0 denotes the zero-field $Z_1 \rightarrow Y_1$ transition energy, i denotes the local site, (+) corresponds to a and (−) corresponds to d , and ${}^g g_i$ denotes the corresponding ground-state effective g value and ${}^e g_i$ the one for the excited state. Similarly, the b and c transition energies are described by

$$E_i^{(b,c)} = E_0 \pm \frac{\mu_B}{2} ({}^g g_i - {}^e g_i) B, \quad (4)$$

and (+) corresponds to transition b and (−) corresponds to c .

In general, the full g tensor can be described by three principal g values in the coordinate frame where the rank-2 tensor is diagonal. For sites of C_2 symmetry, such as in $\text{Er}^{3+}:\text{Y}_2\text{O}_3$, one principal axis, by convention the z axis, must lie along the C_2 symmetry axis. The C_2 g tensor z axis is along [100] for sites 5 and 6, [010] for sites 7 and 8, and [001] for sites 9 and 10. Four parameters completely describe the g tensor: the principal g values g_x , g_y , and g_z along the single-rotation angle α orienting the g tensor $x - y$ principal axes with respect to the crystallographic axes. Each crystal-field level has distinct values of g_x , g_y , and g_z , and the rotation angle α .

Schäfer and Scheller [55] gave the angular dependence of the g values for each magnetically inequivalent C_2 site when the applied field is restricted to a specific high-symmetry crystallographic plane.

When the field is oriented at an angle of Φ in the (001) plane relative to the [100] direction, the effective g values for the six magnetically inequivalent C_2 sites are given by

$$g_{5/6}^2 = g_x^2 \cos^2(\Phi \mp \alpha) + g_y^2 \sin^2(\Phi \mp \alpha), \quad (5)$$

$$g_7^2 = g_8^2 = g_z^2 \sin^2 \Phi + (g_y^2 \cos^2 \alpha + g_x^2 \sin^2 \alpha) \cos^2 \Phi, \quad (6)$$

$$g_9^2 = g_{10}^2 = g_z^2 \cos^2 \Phi + (g_x^2 \cos^2 \alpha + g_y^2 \sin^2 \alpha) \sin^2 \Phi, \quad (7)$$

where g_5 through g_{10} are the effective g values for magnetically inequivalent C_2 sites 5 through 10, respectively. The double indices summarize equations that only differ by a sign of the trigonometric functions; in this case, for Eq. (5) the $(-)$ corresponds to g_5 and $(+)$ corresponds to g_6 .

The angle α is defined as the angle between the x axis and the $\langle 100 \rangle$ crystal axis. Inspecting Eqs. (5) to (7), several key relationships can be found. For example, the ions at sites 7 and 8, with their C_2 axes along [010], and the ions at sites 9 and 10, with their C_2 axes along [001] are magnetically equivalent with respect to the (001) plane. Also, for certain magnetic field directions, principal g values can be measured directly. For example, when the field is oriented at $\Phi = 0$, Eq. (7) reveals that measurement of g_9 and g_{10} yields g_z , while for $\Phi = 90^\circ$, Eq. (6) reveals that g_z can be found from g_7 and g_8 .

When the field is oriented at an angle of Φ in the (110) plane relative to the [001] direction, the equations for the six magnetically inequivalent C_2 sites are given by

$$g_{5/6}^2 = g_z^2 \cos^2(\Phi \mp \alpha) + \left[g_x^2 \cos^2\left(\frac{\pi}{4} \pm \alpha\right) + g_y^2 \sin^2\left(\frac{\pi}{4} \pm \alpha\right) \right] \sin^2 \Phi, \quad (8)$$

$$g_{7/8}^2 = \left(\cos \Phi \cos \alpha \mp \frac{1}{\sqrt{2}} \sin \Phi \sin \alpha \right)^2 g_x^2 + \left(\pm \cos \Phi \sin \alpha + \frac{1}{\sqrt{2}} \sin \Phi \cos \alpha \right)^2 \times g_y^2 + \frac{1}{2} g_z^2 \sin^2 \Phi, \quad (9)$$

$$g_{9/10}^2 = \left(\cos \Phi \cos \alpha \pm \frac{1}{\sqrt{2}} \sin \Phi \sin \alpha \right)^2 g_y^2 + \left(\mp \cos \Phi \sin \alpha + \frac{1}{\sqrt{2}} \sin \Phi \cos \alpha \right)^2 g_x^2 + \frac{1}{2} g_z^2 \sin^2 \Phi. \quad (10)$$

All six sets of ions are orientationally inequivalent with respect to this plane, but special directions can reduce the sixfold inequivalency. The pairs 5 and 6, 7 and 8, and 9 and 10 collapse into three inequivalent sets for $\Phi = 0$. For this direction, g_z can be directly determined from pairs 5 and 6 using Eq. (8). The sites labeled 7 and 8 as well as 9 and 10 become equivalent when $\Phi = \pm 90^\circ$. An interesting case exists for an angle of $\Phi = \pm 54.7^\circ$, where B is along $[\bar{1}11]$

or $[1\bar{1}1]$, as the inequivalence is only twofold with the ions in sites 5, 7, and 9 forming a single equivalent set and the ions in sites 6, 8, and 10 forming another equivalent set. This orientation is especially appealing for applications requiring minimum decoherence and maximum absorption, as will be discussed below.

The g value Eqs. (5) through (10) apply to both the ground- and excited states, with different principal g values g_x , g_y , g_z and angle α . Consequently, the estimated values can be substituted into Eqs. (3) and (4) to predict trial values of the angular dependence of the transition energies. Ground-state g values have been previously measured using EPR [55] and could be used for initial parameters, but excited-state principal g values were unknown. Simulation plots predicting the angular transition-energy dependence provided excellent practical guides for interpreting, assigning, and tracking transitions during data collection. Initial values for the g tensor components were adjusted and plots updated in real time as the data were collected.

To observe individual weaker Zeeman transitions with sufficient signal strength for general orientations where the applied magnetic field lifted the degeneracies, two thicker 0.05% $\text{Er}^{3+}:\text{Y}_2\text{O}_3$ samples were used. One crystal of thickness 8.84 mm was oriented, cut, and polished for applying the magnetic field in the (001) plane while the other had a thickness of 8.25 mm and was used for the (110) plane. All measurements were at $B = 1$ T and $T = 6$ K. All data were captured using laser absorption spectroscopy.

B. Results

Figure 5 shows representative polarization-dependent Zeeman laser absorption scans for B in the (001) plane and B parallel to $\langle 100 \rangle$ at a field of $B = 1$ T with $T = 6$ K. Individual absorption scans have been offset vertically for better visibility. All inner b and c transitions and some of the outer a and d transitions are visible and have been labeled. Outer a (d) transitions for ions in sites 9 and 10 lie at higher (lower) energy as indicated in the transition labeling scheme inset and are therefore outside of the displayed range. Repeating these measurements in 5° increments for the magnetic field direction allowed us to map out the full angular dependence of the a , b , c , and d transitions and to then calculate the corresponding g values.

The full angular dependence of the transition energies when B is constrained to the (001) plane for the 6512 cm^{-1} line in 0.005% $\text{Er}^{3+}:\text{Y}_2\text{O}_3$ at 6 K is shown in Figs. 6 and 7. All four of the Zeeman-split transitions are observed for each site. In this configuration, the 6 magnetically inequivalent C_2 sites (24 lines) are reduced to 4 sites (16 lines). Since the angle α is not zero, there are 3 inequivalent sites (12 lines) for fields along $\langle 001 \rangle$ and $\langle 110 \rangle$ directions, as is clearly evident in Figs. 6 and 7. Solid lines in the figure are calculated as described above using best-fit principal g values presented in Fig. 8.

Figure 8 presents ground- and excited-state g values in the (001) plane; Eqs. (1) and (2) were fit to the (001)-plane g values with results shown as solid lines. Using fitting parameters g_x , g_y , g_z , and α for the ground- and excited states, respectively, the principal g tensor components and α were

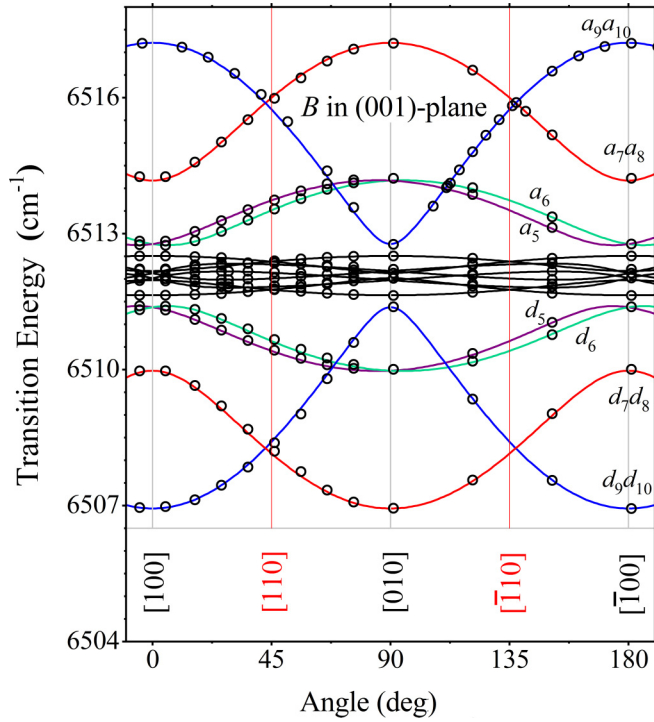


FIG. 6. Orientation dependence of the Zeeman transitions at $T = 6$ K and $B = 1$ T for C_2 sites when \mathbf{B} is constrained to a (001) plane. Symbols are experimental data. Solid lines are calculated from best fit to g values. The outer a and d transitions have been labeled with the subscript, giving the magnetic inequivalent sites. The solid black lines that correspond to inner b and c transitions are expanded in Fig. 7 for better clarity. The special field orientation for minimizing decoherence in this plane is for $\mathbf{B} \parallel \langle 110 \rangle$ and has been indicated by red vertical lines.

extracted for Z_1 and Y_1 and are summarized in Table II. From Fig. 8 the g_z principal value can also be read directly from the maxima and the rotation angles are evident in the lowest two curves. The $\langle 110 \rangle$ or $\langle \bar{1}10 \rangle$ directions are determined to be the most appealing applied-field directions for practical applications as explained in detail in the next section below, and they are labeled with red vertical lines.

Inspecting the values in Table II, our fitted ground-state g tensor components agree well with Schäfer and Scheller's EPR measurements. For the ground state, Schäfer and Scheller's EPR measurement yielded $g_z = 12.314$, $g_x = 1.645$, $g_y = 4.892$, and $\alpha = \pm 2^\circ$ [55]. Our results demonstrate that optical methods can accurately determine g values as an alternative approach to EPR. The excited-state principal g values are not accessible by EPR. Inspecting Table II, note that the ground- and excited states not only have different g values, but they also have different rotation angles α . The angle for the excited state is larger in magnitude and also rotated in the opposite sense about the $\langle 100 \rangle$ axis as compared to the ground-state angle.

To confirm our C_2 -site g tensor components determined from the (001)-plane spectra, we also measured the angular-dependent Zeeman transition energies with the magnetic field varying in the orthogonal (110) plane. Results are shown in Figs. 9 and 10. Solid lines represent the expected behavior

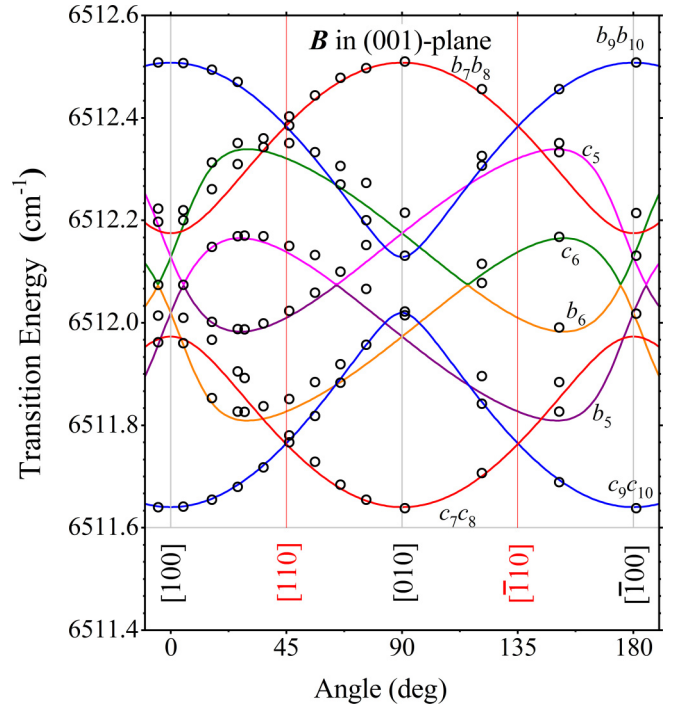


FIG. 7. Detail of orientation dependence of the b and c Zeeman transitions at $T = 6$ K and $B = 1$ T for C_2 sites when \mathbf{B} is constrained to the (001) plane. Symbols are experimental data. Solid lines are calculated from best fit to g values. Small disagreements between fit and data are attributed to a slight misalignment of the sample. The inner b and c transitions have been labeled with the subscript, giving the magnetic inequivalent sites. The special field orientation for minimizing decoherence in this plane is $\mathbf{B} \parallel \langle 110 \rangle$, which is indicated by red vertical lines.

for these transitions based on the g values derived from the (001)-plane data. As can be observed from Figs. 9 and 10, in this configuration there are 6 magnetically inequivalent C_2 sites generally, collapsing into 4 along $\langle 110 \rangle$, 3 along $\langle 001 \rangle$, and 2 along $\langle 111 \rangle$ directions. The $\langle 111 \rangle$ direction is the most appealing direction for practical applications and will be discussed further in the next section.

Figure 11 presents the (110)-plane ground- and excited-state g values; solid curves again show the expected behavior based on the g tensor components determined from the (001) plane. Note that the sixfold orientational equivalence with respect to $\langle 110 \rangle$ is more easily observed in the excited state than in the ground state, because the tipping angle α is nearly zero in the ground state.

C. Discussion

As described above, minimizing decoherence of the optically active Er^{3+} ions requires the application of a magnetic field to “freeze out” unwanted spin-flip transitions that lead to spectral diffusion. The resulting transition-frequency shifts for Er^{3+} ion populations in the various magnetically inequivalent sites are governed by the g values for each site as a function of magnetic field strength and orientation. The strategy for optimizing the applied field is to maximize the ground-state $^4I_{15/2} (Z_1)$ and excited-state $^4I_{13/2} (Y_1)$ splittings for the largest

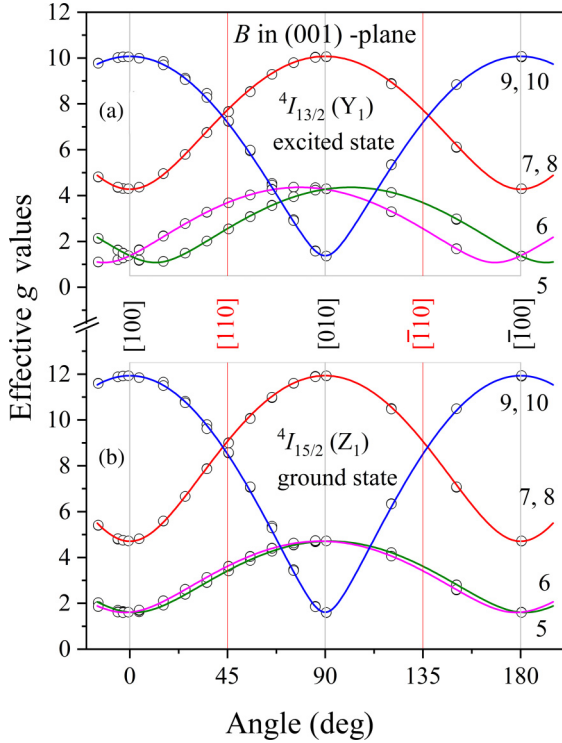


FIG. 8. Effective g values for C_2 site with \mathbf{B} in the (001) plane for the lowest-energy ${}^4I_{15/2}(Z_1)$ and ${}^4I_{13/2}(Y_1)$ states of $\text{Er}^{3+}:\text{Y}_2\text{O}_3$. Symbols are data calculated from Zeeman spectra of Fig. 6 and 7 and using Eqs. (3) and (4); solid lines are best fits. The special field orientation for minimizing decoherence in this plane is $\mathbf{B} \parallel \langle 110 \rangle$ as indicated by red vertical lines.

population of coherently interacting ions, while at the same time maximizing the ground-state splittings for all non-participating ions—those with different transition energies, including ions in C_{3i} sites [35]. These optimization strategies applied in a complicated system like $\text{Er}^{3+}:\text{Y}_2\text{O}_3$ are often incompatible. In that case, the angular-dependent g value data guide the tradeoffs surrounding choice of external magnetic field direction and magnitude to minimize decoherence.

According to these arguments, both the (110) and the (001) planes offer choices for magnetic field application to minimize decoherence. We identified two optimum magnetic field orientations—one for each plane.

TABLE II. Er^{3+} principal g values for ions in C_2 symmetry as determined from angle-dependent Zeeman absorption. Included is the special case of g values along $\langle 111 \rangle$ where two sets of ions at sites 5, 7, 9 and at 6, 8, 10, each consisting of half of the C_2 ions, are each orientationally equivalent with respect to $\langle 111 \rangle$ with eight possible transitions.

Level		C_2 site				α
		g_x [100]	g_y [010]	g_z [001]	g $\langle 111 \rangle$	
${}^4I_{13/2}$	Y_1	1.08	4.36	10.07	6.18 and 6.54	-11.7°
${}^4I_{15/2}$	Z_1	1.60	4.71	11.93	7.43 [$\bar{1}11$] 7.50 [$\bar{1}\bar{1}\bar{1}$]	2.06°

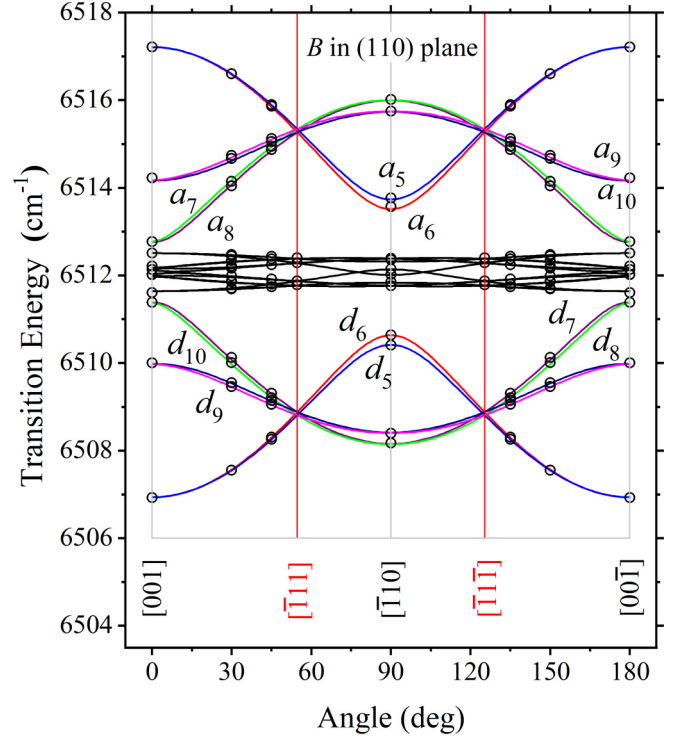


FIG. 9. Orientation dependence of the Zeeman transitions at $T = 6$ K and $B = 1$ T for C_2 sites when \mathbf{B} is constrained to a (110) plane. The “outer transitions” have been labeled. Solid lines are calculated from best fit to g values. The inner b and c transitions are expanded in Fig. 10. The special field orientations for minimizing decoherence in this plane are $\mathbf{B} \parallel \langle 111 \rangle$, as indicated with red vertical lines.

The most promising orientation for applying a magnetic field is along $\langle 111 \rangle$ in the (110) plane using the b transition, which for this orientation has an energy of 6512.22 cm^{-1} at $B = 1$ T. This special orientation has been marked by red vertical lines in Figs. 9–11. Following an examination of Fig. 11 for the g value angular dependence, half of the ions in C_2 sites constitute the optically active ions while the other half constitute environmental ions as a consequence of the twofold inequivalence of C_2 sites for this orientation. As can be seen from Fig. 9, as well as Fig. 11 and Table II, all C_2 -site ground-state ${}^4I_{15/2}(Z_1)$ g values are 7.43 along $[\bar{1}11]$ and 7.50 along $[\bar{1}\bar{1}\bar{1}]$ in this orientation. The excited-state C_2 -site ${}^4I_{13/2}(Y_1)$ g values are divided into two populations: one with a g value of 6.18 and the other with 6.54. As will be reported elsewhere, the C_{3i} sites form two inequivalent groups in this orientation; one-fourth (three-fourths) of these environmental ions have a very high (moderate) ground-state C_{3i} -site ${}^4I_{15/2}(Z_1)$ g value of 12.2 (5.1) or higher [53]. At relatively low overall doping and relatively low magnetic field, the upper components of the ground states for both the optically active and environmental ions are depopulated. Spin flips are minimized on both C_2 and C_{3i} sites for this field orientation.

A second orientation suggested by the data applies the magnetic field in the (001) plane along $\langle 110 \rangle$ for which the b transition occurs at 6512.38 cm^{-1} at $B = 1.0$ T. This orientation is indicated by red lines in Figs. 6–8. Ions in sites labeled (7, 8) and (9, 10) are equivalent in pairs for applied fields in this plane. Ground- (excited-) g values for ions in all

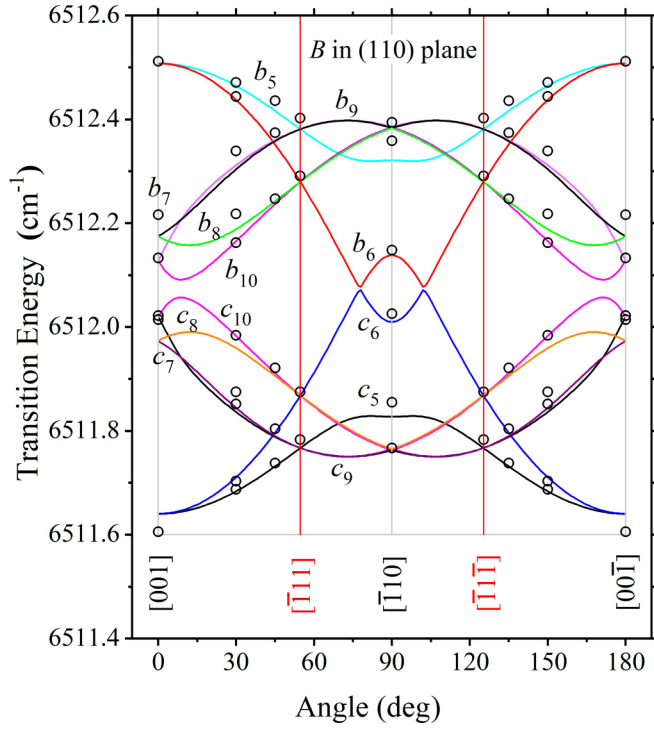


FIG. 10. Detail of the orientation dependence of the b and c Zeeman transitions at $T = 6$ K and $B = 1$ T for C_2 sites when \mathbf{B} is constrained to a (110) plane. Solid lines are calculated from best fit to g values. The special field orientations for minimizing decoherence in this plane are $\mathbf{B} \parallel \langle 111 \rangle$ and have been labeled with red vertical lines.

four sites for \mathbf{B} parallel to $\langle 110 \rangle$ are 8.8 (7.5). Two-thirds of the ions in C_2 sites constitute the optically active ions with very high ground- and excited-state g values; only one-third of the ions in C_2 sites contribute to the environment but have lower ground-state g values (3.4 and 3.6). As will be reported elsewhere, ions in C_{3i} sites are inequivalent in this orientation and one-half of these environment ions have a very high ground-state g value of 10.1; however, the remaining half of these environment ions have a lower ground-state g value of 3.3 [53,55]. In summary, this orientation requires the lowest overall doping due to the large fraction of ions in C_2 sites utilized as optically active ions (2/3), but a larger magnetic field is required to depopulate the upper Zeeman component of the ground state due to low g values for these ions in C_2 and C_{3i} sites.

We should also note that the quadratic Zeeman effect can affect the magnetic splittings and spin dynamics at higher magnetic field strengths, depending on the separation between crystal-field levels [69,70]. We expect these effects to be small for this material over the range of magnetic field strengths studied here due to the relatively large crystal-field splittings of 39.5 and 32.4 cm^{-1} in the ground- and excited states, respectively, as determined from Table I.

V. PHOTON ECHOES AND SPECTRAL DIFFUSION

The optical decoherence of Er^{3+} ions at C_2 -point symmetry sites was measured from two-pulse photon-echo decays to confirm the optimum direction for applying a magnetic field.

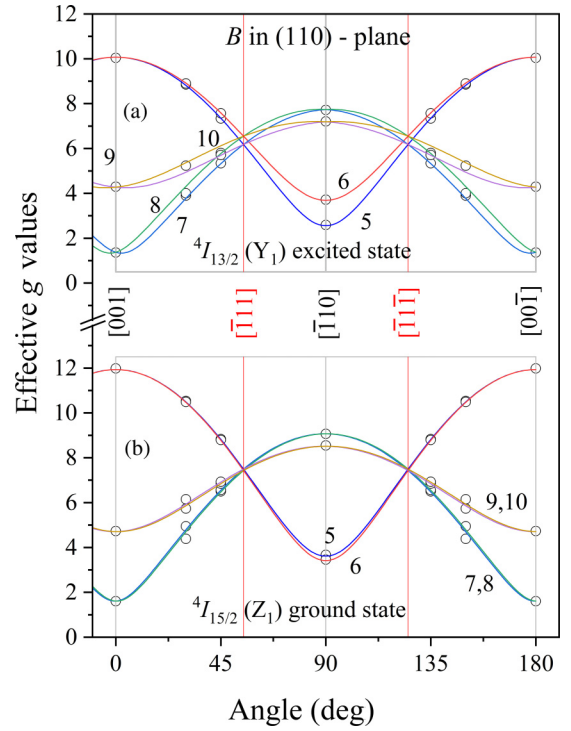


FIG. 11. Effective g value variations of the C_2 site for the case of \mathbf{B} in the (110) plane for the lowest-energy ${}^4I_{15/2}$ (Z_1) and ${}^4I_{13/2}$ (Y_1) states of $\text{Er}^{3+}:\text{Y}_2\text{O}_3$. Symbols are data calculated from Zeeman spectra of Figs. 9 and 10 and using Eqs. (1) and (2); solid lines are best fits. The special field orientations for minimizing decoherence in this plane are $\mathbf{B} \parallel \langle 111 \rangle$ and have been labeled with red vertical lines.

A. Experiment

Two-pulse echo decays were measured for the b transition in 0.005% $\text{Er}^{3+}:\text{Y}_2\text{O}_3$ as a function of magnetic field strength for two magnetic field directions. First, we chose the magnetic field along the optimum direction with \mathbf{B} parallel to $\langle 111 \rangle$ in the (110) plane and then contrasted that result with the case of \mathbf{B} parallel to $\langle 110 \rangle$. The phase-memory lifetime T_M is the time over which the initial intensity decays to I_0/e^2 and was extracted from the measured echo decays as a function of magnetic field strength for both orientations. The phase lifetimes were then used to calculate the effective homogeneous linewidth Γ_h .

The experimental photon-echo setup was similar to the one described in Refs. [30] and [31]. The crystal was immersed in a superfluid liquid helium bath held at $T = 1.8$ K using an Oxford Instruments Spectromag cryostat, and the laser light propagated with \mathbf{k} parallel to $\langle 110 \rangle$. The ECDL output power of ~ 1.8 mW was amplified by an erbium-doped fiber amplifier. A 165-MHz acousto-optic modulator (AOM) gated the amplified laser beam to generate pulses for two-pulse echo excitation, with pulse widths of 860 ns and 1.56 μs . An 80-MHz gating AOM after the crystal was used to discriminate the echo signal from the excitation pulses. The echo signal was detected using a fast amplified InGaAs photodiode and processed with a digital oscilloscope interfaced with a data-acquisition computer that recorded the integrated area

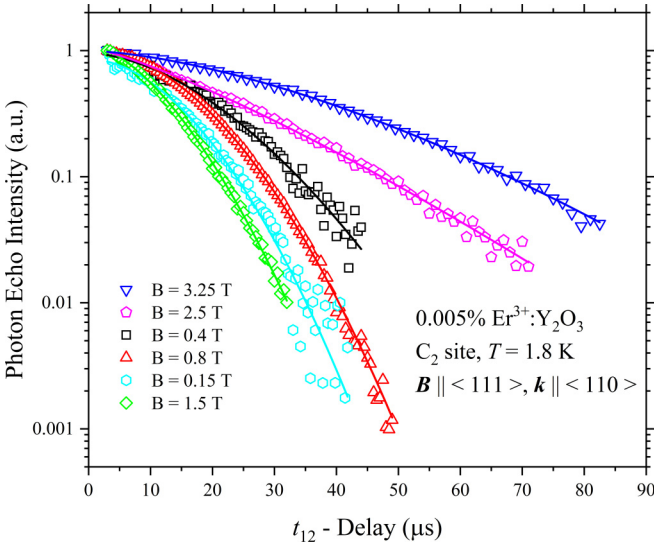


FIG. 12. Two-pulse photon-echo decays of the C_2 site in 0.005% $\text{Er}^{3+}:\text{Y}_2\text{O}_3$ at $T = 1.8$ K as a function of magnetic field strengths with $\mathbf{B} \parallel \langle 111 \rangle$ and $\mathbf{k} \parallel \langle 110 \rangle$. Solid lines are least-square fits of the empirical Mims function to the data (see text).

of the echo signal as a function of the pulse separation in the two-pulse excitation sequence. Two-pulse photon-echo decays were measured for magnetic fields up to $B = 4.5$ T. For the C_2 site at low magnetic field strengths of $B < 0.3$ T, a modulation was observed in the two-pulse echo decays that was attributed to superhyperfine coupling between Er^{3+} and neighboring ^{89}Y nuclear spins, making the analysis of decays more difficult. At these low fields, the echo-pulse sequence simultaneously excites transitions from multiple superhyperfine levels, producing a coherent interference that causes the echo-decay modulation. This effect has also been observed in other Er^{3+} -doped materials, such as $\text{Er}^{3+}:\text{Y}_2\text{SiO}_5$ [30] and $\text{Er}^{3+}:\text{KTP}$ [31], as well as for other materials doped with paramagnetic ions, such as $\text{Yb}^{3+}:\text{YAG}$ (yttrium aluminum garnet) [71].

B. Results

Figure 12 shows representative C_2 -site two-pulse echo-decay curves for several magnetic field strengths with \mathbf{B} parallel to $\langle 111 \rangle$. At zero field, the photon echo was observable but very weak. The echo intensity increased by an order of magnitude when a small magnetic field of $B = 0.1$ T was applied. From the figure, the observed echo decays were nonexponential, indicating time-dependent decoherence due to the presence of spectral diffusion during the echo-pulse sequence.

We analyzed the echo-decay curves in Fig. 12 using the empirical Mims equation [72]:

$$I = I_0 \exp \left\{ -2 \left(\frac{2t_{12}}{T_M} \right)^x \right\}, \quad (5)$$

where I_0 is the initial echo intensity, t_{12} is the separation between pulse 1 and pulse 2, and x is an empirical parameter that depends on the spectral diffusion dynamics that determine the shape of the echo-decay curve. The $1/e$ phase-coherence

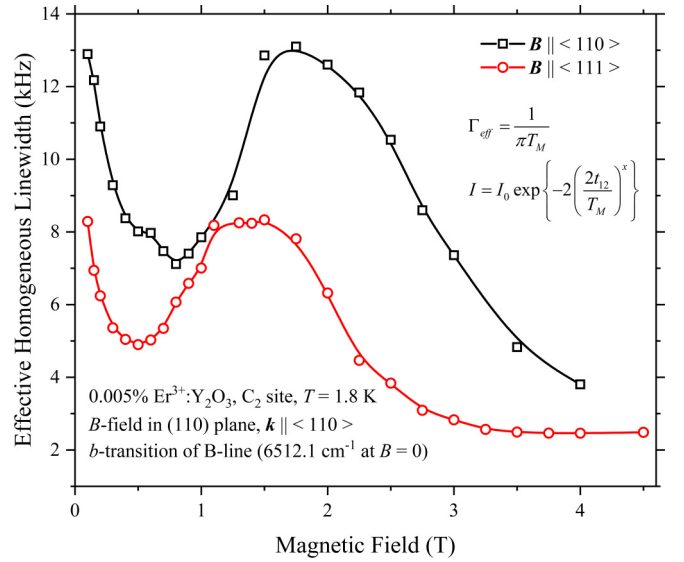


FIG. 13. Dependence of effective homogeneous linewidth on magnetic field strength for the C_2 -site Er^{3+} ions in 0.005% $\text{Er}^{3+}:\text{Y}_2\text{O}_3$ at $T = 1.8$ K with $\mathbf{B} \parallel \langle 111 \rangle$ contrasted with $\mathbf{B} \parallel \langle 110 \rangle$. Symbols correspond to experimental data, and solid lines have been drawn to guide the eye (see text).

lifetime T_M obtained using Eq. (5) is the time over which the initial intensity decays to I_0/e^2 . Solid lines in Fig. 12 are fits to Eq. (5). The effective homogeneous linewidth Γ_h over the timescale of the echo-decay measurement can be defined in terms of T_M using the relation

$$\Gamma_h = \frac{1}{\pi T_M}. \quad (6)$$

Figure 13 shows the variation of the effective homogeneous linewidth Γ_h for C_2 -site Er^{3+} ions as a function of magnetic field strength; solid lines in the graph have been drawn to guide the eye. The cases of $\mathbf{B} \parallel \langle 110 \rangle$ and $\mathbf{B} \parallel \langle 111 \rangle$ are plotted in the same graph for comparison. Narrow linewidths of several kilohertz were observed for all field strengths in both cases, but for the case of \mathbf{B} parallel to $\langle 111 \rangle$, the effective homogeneous linewidth was significantly narrower than that for parallel to $\langle 110 \rangle$, which agrees with our expectation that $\langle 111 \rangle$ is the preferred magnetic field direction.

As these results show, the C_2 -site g value variations can serve as a guide to determine that the optimal direction for applying an external magnetic field in the (110) plane is when \mathbf{B} is parallel to $\langle 111 \rangle$. Using this magnetic field direction, two-pulse photon echoes gave a homogeneous linewidth of 5 kHz for an applied magnetic field of 0.5 T, narrowing and saturating at 2.5 kHz at 3.5 T. Along this axis, the C_2 -site g values from Fig. 11 are 7.495 and 7.433 for the ground state and 6.180 and 6.551 for the excited state, while the C_{3i} -site g values are all 5.1 or higher as we will report elsewhere [53]. Large g values lead to freezing out of electron-spin fluctuations and reduced magnetic ion-ion interactions and, consequently, narrower effective homogeneous linewidths. In contrast for \mathbf{B} parallel to $\langle 001 \rangle$, only 2 of the 6 subsets of ions in the ground state have large g values of 11.9, while the

others are 4.7 and 1.6, too small to thermally freeze out their population to the same degree.

We also note that the variation of the effective homogeneous linewidth with magnetic field strength shows a substantial increase at intermediate fields for both directions that appears as a characteristic “bump” in the overall trends. This bump feature was also observed in $\text{Er}^{3+}:\text{Y}_2\text{SiO}_5$ [30,51,73], $\text{Er}^{3+}:\text{LiNbO}_3$ [67], and $\text{Er}^{3+}:\text{KTP}$ [31], as well as in other paramagnetic rare-earth materials such as $\text{Yb}^{3+}:\text{YAG}$ [71] and $\text{Nd}^{3+}:\text{YVO}_4$ [73]. In general, it arises from the interplay between the magnitude and rate of the spectral diffusion mechanism that predominantly determines the overall observed behavior for the effective homogeneous linewidth for these Er^{3+} concentrations. This behavior can be quantitatively described, and individual spin-flip processes can be identified, as shown in the references cited above; however, the many magnetically inequivalent sites and the presence of two crystallographically inequivalent sites requires a large number of parameters to describe in this case, requiring more extensive stimulated photon-echo decay measurements to quantitatively analyze the spectral diffusion dynamics [30]. It should be noted that we have found no evidence for decoherence due to TLS in these crystals so we expect the coherence at high fields to be likely limited by the yttrium nuclear spins in the lattice.

VI. CONCLUSION

The results presented here provide an overview of the spectroscopic, magnetic, and decoherence properties of Er^{3+} ions occupying C_2 symmetry sites in Y_2O_3 that are relevant for quantum information science, spectral hole burning, and spatial-spectral holography applications. The C_2 -site $\text{Er}^{3+} \ ^4I_{15/2} \leftrightarrow \ ^4I_{13/2}$ transition occurs at a convenient laser-accessible wavelength of 1536 nm suitably located in the telecom C band where off-the-shelf optical hardware is well developed and direct interfacing of the material with existing telecom infrastructure is possible.

Using site-selective spectroscopy, the crystal-field level structure of the $\ ^4I_{15/2}$ ground-state and $\ ^4I_{13/2}$ excited-state multiplets were determined. The fluorescence lifetime of the $\ ^4I_{13/2}$ excited state was measured as 8.5 ms. Laser absorption revealed an inhomogeneous linewidth of 780 MHz in the 0.005% $\text{Er}^{3+}:\text{Y}_2\text{O}_3$ material.

Using angular-dependent high-resolution Zeeman laser absorption spectroscopy, we determined the complete electronic

g tensors and their orientations for both the $\ ^4I_{15/2}$ (1) ground state and the $\ ^4I_{13/2}$ (1) excited state for Er^{3+} ions occupying the C_2 -symmetry lattice sites. Our independently measured g tensor results for the ground state, obtained by high-resolution optical spectroscopy, agree well with earlier work using microwave EPR spectroscopy, while the excited-state g tensor components provide useful material information. Our optical measurements give comparable precision to EPR methods and provide a useful alternative approach for measuring g tensors for both ground- and excited states. The experimental measurements reported here are directly relevant to development of SHB materials and optical systems for quantum information science. From our results, we find that decoherence is generally minimized by employing materials with weakly magnetic or nonmagnetic host constituents such as Y_2O_3 and then choosing applied magnetic field directions where both the excited- and ground-state g values of the active ion and the effective g values of any other perturbing environmental spins in the ground state are all simultaneously maximized. The longest decoherence times were measured with the magnetic field in the (110) crystal plane along (111). This direction gave overall maxima of all effective g values for both ground- and excited states and maximized magnetic equivalence of optically active ions while effective g values of environmental ions were also large.

Two-pulse echo-decay measurements also revealed the presence of spectral diffusion due to direct phonon-driven magnetic dipole-dipole interactions between the Er^{3+} ions, as has been observed in other Er^{3+} systems such as $\text{Er}^{3+}:\text{Y}_2\text{SiO}_5$ [30] and $\text{Er}^{3+}:\text{KTP}$ [31].

Overall, our results demonstrate that $\text{Er}^{3+}:\text{Y}_2\text{O}_3$ is a suitable material system for many photonic and quantum information science applications. A follow-up publication will describe the properties of Er^{3+} ions at the C_{3i} site in $\text{Er}^{3+}:\text{Y}_2\text{O}_3$.

ACKNOWLEDGMENTS

This material is based on work supported in part by AFOSR Grant No. F49620-98-1-0171. Work by T.B. and R.L.C. was supported in part by National Science Foundation Grant No. OMA-1936350. Work by C.W.T. was supported in part by the Department of Energy, Office of Basic Energy Sciences, Division of Materials Sciences and Engineering under Grant No. DE-SC0019406.

-
- [1] N. Ohlsson, R. K. Mohan, and S. Kröll, *Opt. Commun.* **201**, 71 (2002).
 - [2] H. De Riedmatten, M. Afzelius, M. U. Staudt, C. Simon, and N. Gisin, *Nature (London)* **456**, 773 (2008).
 - [3] W. Tittel, M. Afzelius, T. Chanelière, R. Cone, S. Kröll, S. Moiseev, and M. Sellars, *Laser Photonics Rev.* **4**, 244 (2010).
 - [4] C. Simon, M. Afzelius, J. Appel, A. B. de La Giroday, S. Dewhurst, N. Gisin, C. Hu, F. Jelezko, S. Kröll, and J. Müller, *Eur. Phys. J. D* **58**, 1 (2010).
 - [5] M. Afzelius, I. Usmani, A. Amari, B. Lauritzen, A. Walther, C. Simon, N. Sangouard, J. Minář, H. de Riedmatten, N. Gisin, and S. Kroll, *Phys. Rev. Lett.* **104**, 040503 (2010).
 - [6] M. P. Hedges, J. J. Longdell, Y. Li, and M. J. Sellars, *Nature (London)* **465**, 1052 (2010).
 - [7] C. W. Thiel, T. Böttger, and R. L. Cone, *J. Lumin.* **131**, 353 (2011).
 - [8] E. Saglamyurek, N. Sinclair, J. Jin, J. A. Slater, D. Oblak, F. Bussièeres, M. George, R. Ricken, W. Sohler, and W. Tittel, *Nature (London)* **469**, 512 (2011).
 - [9] T. Zhong, J. M. Kindem, J. G. Bartholomew, J. Rochman, I. Craiciu, E. Miyazono, M. Bettinelli, E. Cavalli, V. Verma, and S. W. Nam, *Science* **357**, 1392 (2017).
 - [10] A. M. Dibos, M. Raha, C. M. Phenicie, and J. D. Thompson, *Phys. Rev. Lett.* **120**, 243601 (2018).

- [11] Z. Cole, T. Böttger, R. Krishna Mohan, R. Reibel, W. R. Babbitt, R. L. Cone, and K. D. Merkel, *Appl. Phys. Lett.* **81**, 3525, (2002).
- [12] W. R. Babbitt, Z. W. Barber, S. H. Bekker, M. D. Chase, C. Harrington, K. D. Merkel, R. K. Mohan, T. Sharpe, C. R. Stiffler, A. S. Traxinger, and A. J. Woitke, *Laser Phys.* **24**, 094002 (2014).
- [13] Z. W. Barber, C. Harrington, R. K. Mohan, T. Jackson, C. Stiffler, P. B. Sellin, and K. D. Merkel, *Appl. Optics* **56**, 5398 (2017).
- [14] M. Colice, F. Schlottau, and K. H. Wagner, *Appl. Opt.* **45**, 6393 (2006).
- [15] P. Berger, Y. Attal, M. Schwarz, S. Molin, A. Louchet-Chauvet, and T. Chanelière, *J. Lightwave Technol.* **34**, 4658 (2016).
- [16] A. Louchet-Chauvet, P. Berger, P. Nouchi, D. Dolfi, A. Ferrier, P. Goldner, and L. Morvan, *Laser Phys.* **30**, 066203 (2020).
- [17] P. B. Sellin, N. M. Strickland, T. Böttger, J. L. Carlsten, and R. L. Cone, *Phys. Rev. B* **63**, 155111 (2001).
- [18] T. Böttger, G. J. Pryde, and R. L. Cone, *Opt. Lett.* **28**, 200 (2003).
- [19] M. Thorpe, L. Rippe, T. Fortier, M. S. Kirchner, and T. Rosenband, *Nat. Photonics* **5**, 688 (2011).
- [20] C. W. Thiel, R. L. Cone, and T. Böttger, *J. Lumin.* **152**, 84 (2014).
- [21] N. Kunkel, A. Ferrier, C. W. Thiel, M. O. Ramírez, L. E. Bausá, R. L. Cone, A. Ikesue, and P. Goldner, *APL Mater.* **3**, 096103 (2015).
- [22] A. Kinos, Q. Li, L. Rippe, and S. Kröll, *Appl. Opt.* **55**, 10442 (2016).
- [23] C. O'Brien, N. Lauk, S. Blum, G. Morigi, and M. Fleischhauer, *Phys. Rev. Lett.* **113**, 063603 (2014).
- [24] X. Fernandez-Gonzalvo, S. P. Horvath, Y.-H. Chen, and J. J. Longdell, *Phys. Rev. A* **100**, 033807 (2019).
- [25] S. Welinski, P. J. T. Woodburn, N. Lauk, R. L. Cone, C. Simon, P. Goldner, and C. W. Thiel, *Phys. Rev. Lett.* **122**, 247401 (2019).
- [26] J. G. Bartholomew, J. Rochman, T. Xie, J. M. Kindem, A. Ruskuc, I. Craiciu, M. Lei, and A. Faraon, *Nat. Commun.* **11**, 3266 (2020).
- [27] T. Chanelière, R. Dardaillon, P. Lemonde, J. J. Viennot, P. Bertet, E. Flurin, P. Goldner, and D. Serrano, *J. Luminescence* **272**, 120647 (2024).
- [28] S. Wang, L. Yang, R. L. Cone, C. W. Thiel, and H. X. Tang, *Phys. Rev. Appl.* **18**, 014071 (2022).
- [29] K. Heshami, D. G. England, P. C. Humphreys, P. J. Bustard, V. M. Acosta, J. Nunn, and B. J. Sussman, *J. Mod. Opt.* **63**, 2005 (2016).
- [30] T. Böttger, C. W. Thiel, Y. Sun, and R. L. Cone, *Phys. Rev. B* **73**, 075101 (2006).
- [31] T. Böttger, C. W. Thiel, Y. Sun, R. M. MacFarlane, and R. L. Cone, *J. Lumin.* **169**, 466 (2016).
- [32] N. Kukharchyk, D. Sholokhov, O. Morozov, S. Korableva, A. Kalachev, and P. Bushev, *New J. Phys.* **20**, 023044 (2018).
- [33] I. Craiciu, M. Lei, J. Rochman, J. M. Kindem, J. G. Bartholomew, E. Miyazono, T. Zhong, N. Sinclair, and A. Faraon, *Phys. Rev. Appl.* **12**, 024062 (2019).
- [34] T. Böttger, C. W. Thiel, R. L. Cone, and Y. Sun, *Phys. Rev. B* **77**, 155125 (2008).
- [35] T. Böttger, C. W. Thiel, R. L. Cone, and Y. Sun, *Phys. Rev. B* **79**, 115104 (2009).
- [36] J. B. Gruber, R. P. Leavitt, C. A. Morrison, and N. C. Chang, *J. Chem. Phys.* **82**, 5373 (1985).
- [37] M. B. Korzenski, P. Lecoeur, and B. Mercey, *Appl. Phys. Lett.* **78**, 1210 (2001).
- [38] C. W. Thiel, Y. Sun, R. M. Macfarlane, T. Böttger, and R. L. Cone, *J. Phys. B: At. Mol. Opt. Phys.* **45**, 124013 (2012).
- [39] G. Corrielli, A. Seri, M. Mazzerà, R. Osellame, and H. de Riedmatten, *Phys. Rev. Appl.* **5**, 054013 (2016).
- [40] M. F. Askarani, M. I. G. Puigibert, T. Lutz, V. B. Verma, M. D. Shaw, S. W. Nam, N. Sinclair, D. Oblak, and W. Tittel, *Phys. Rev. Appl.* **11**, 054056 (2019).
- [41] R. M. Macfarlane, F. Könz, Y. Sun, and R. L. Cone, *J. Lumin.* **86**, 311 (2000).
- [42] C. W. Thiel, N. Sinclair, W. Tittel, and R. L. Cone, *Phys. Rev. B* **90**, 214301 (2014).
- [43] T. Lutz, L. Veissier, C. W. Thiel, P. J. T. Woodburn, R. L. Cone, P. E. Barclay, and W. Tittel, *Sci. Tech. Adv. Mater.* **17**, 63 (2016).
- [44] T. Lutz, L. Veissier, C. W. Thiel, P. J. T. Woodburn, R. L. Cone, P. E. Barclay, and W. Tittel, *J. Lumin.* **191**, 2 (2017).
- [45] H. Zhang, J. Yang, S. Gray, J. A. Brown, T. D. Ketcham, D. E. Baker, A. Carapella, R. W. Davis, J. G. Arroyo, and D. A. Nolan, *ACS Omega* **2**, 3739 (2017).
- [46] A. Ferrier, C. W. Thiel, B. Tumino, M. O. Ramirez, L. E. Bausá, R. L. Cone, A. Ikesue, and P. Goldner, *Phys. Rev. B* **87**, 041102(R) (2013).
- [47] S. Liu, A. Fossati, D. Serrano, A. Tallaire, A. Ferrier, and P. Goldner, *ACS Nano* **14**, 9953 (2020).
- [48] N. Sinclair, D. Oblak, C. W. Thiel, R. L. Cone, and W. Tittel, *Phys. Rev. Lett.* **118**, 100504 (2017).
- [49] M. K. Singh, A. Prakash, G. Wolfowicz, J. Wen, Y. Huang, T. Rajh, D. D. Awschalom, T. Zhing, and S. Guha, *APL Mater.* **8**, 031111 (2020).
- [50] A. Ferrier, N. Harada, M. Scarafagio, E. Briand, J. J. Ganem, I. Vickridge, A. Seyeux, P. Marcus, D. Serrano, P. Goldner, and A. Tallaire, *J. Phys. Chem. C* **124**, 19725 (2020).
- [51] R. M. Macfarlane, T. L. Harris, Y. Sun, and R. L. Cone, and R. W. Equall, *Optics Lett.* **22**, 871 (1997).
- [52] R. M. Macfarlane and R. M. Shelby, *Opt. Commun.* **39**, 169 (1981).
- [53] T. Böttger, G. D. Reinemer, R. L. Cone, and C. W. Thiel (unpublished).
- [54] Y. Sun, T. Böttger, C. W. Thiel, and R. L. Cone, *Phys. Rev. B* **77**, 085124 (2008).
- [55] G. Schäfer and S. Scheller, *Phys. Kondens. Mater.* **5**, 48 (1966).
- [56] L. Pauling and M. D. Shappell, *Z. Kristallogr.* **75**, 128 (1930).
- [57] M. Mandel, *Appl. Phys. Lett.* **2**, 197 (1963).
- [58] W. F. Krupke, *Phys. Rev.* **145**, 325 (1966).
- [59] T. Böttger, C. W. Thiel, Y. Sun, and R. L. Cone, *Phys. Rev. B* **74**, 075107 (2006).
- [60] W. F. K. Kisliuk and J. B. Gruber, *J. Chem. Phys.* **40**, 3606 (1964).
- [61] N. C. Chang, J. B. Gruber, R. P. Leavitt, and C. A. Morrison, *J. Chem. Phys.* **76**, 3877 (1982).
- [62] J. B. Gruber, W. F. Krupke, and J. M. Poindexter, *J. Chem. Phys.* **41**, 3363 (1964).
- [63] J. R. Dean and D. Bloor, *J. Phys. C: Solid State Phys.* **5**, 2921 (1972).

- [64] G. H. Dieke, Spectra and energy levels of rare earth ions in crystals, in *InterScience* (Johan Wiley and Sons, New York, 1968).
- [65] D. S. Sumida and T. Y. Fan, *Opt. Lett.* **19**, 1343 (1994).
- [66] J. A. Muñoz, B. Herreros, G. Lifante, and F. Cussó, *Phys. Stat. Sol. A* **168**, 525 (1998).
- [67] C. W. Thiel, R. M. Macfarlane, T. Böttger, Y. Sun, R. L. Cone, and W. R. Babbitt, *J. Lumin.* **130**, 1603 (2010).
- [68] C. W. Thiel, T. Böttger, W. R. Babbitt, and R. L. Cone, *J. Lumin.* **130**, 1598 (2010).
- [69] L. Veissier, C. W. Thiel, T. Lutz, P. E. Barclay, W. Tittel, and R. L. Cone, *Phys. Rev B* **94**, 205133 (2016).
- [70] J. H. Davidson, A. Das, N. Alfasi, R. L. Cone, C. W. Thiel, and W. Tittel, *Phys. Rev. B* **107**, 094105 (2023).
- [71] T. Böttger, C. W. Thiel, R. L. Cone, Y. Sun, and A. Faraon, *Phys. Rev. B* **94**, 045134 (2016).
- [72] W. B. Mims, *Phys. Rev.* **168**, 370 (1968).
- [73] Y. C. Sun, in *Spectroscopic Properties of Rare Earths in Optical Materials*, edited by G. Liu and B. Jacquier (Springer, Berlin, and Tsinghua University Press, Beijing, 2005), pp. 379–429.